ACS APPLIED MATERIALS & INTERFACES

Research Article

Cite This: ACS Appl. Mater. Interfaces 2020, 12, 1024−1035

www.acsami.org

Scrutinizing the Pore Chemistry and the Importance of Cu(I) Defects in TCNQ-Loaded $Cu_3(BTC)_2$ by a Multitechnique Spectroscopic Approach

Christian Schneider,[†] Matthias Mendt,[‡] Andreas Pöppl,[‡] Valentina Crocellà,*[,§] and Roland A. Fischer*[,†]

[†]Department of Chemistry, Technical University of Munich, Lichtenbergstrasse 4, D-85748 Garching, Germany

[‡]Felix Bloch Institute for Solid State Physics, University Leipzig, Linnéstrasse 5, D-04103 Leipzig, Germany

[§]Department of Chemistry, NIS and INSTM Reference Centre, Università di Torino, Via G. Quarello 15, I-10135 and Via P. Giuria 7, I-10125 Torino, Italy

Supporting Information

ABSTRACT: Host−guest interactions control the fundamental processes in porous materials for many applications such as gas storage and catalysis. The study of these processes, however, is not trivial, even if the material is crystalline. In particular, metal−organic frameworks (MOFs) represent a complex situation since guest molecules can interact with different parts of the organic linkers and the metal clusters and may alter the details of the pore structure and system properties. A prominent example is the so-called retrofitted MOF material TCNQ@$Cu_3(BTC)_2$ that has attracted a lot of attention due to its electronic properties induced by the host−guest interactions. Only recently, structural evidence has been presented for a bridging binding mode of TCNQ to two Cu paddlewheel units; however, many issues regarding the redox chemistry of $Cu_3(BTC)_2$ and TCNQ are currently unsolved. Herein, we report a powerful spectroscopic approach to study the host−guest chemistry of this material. Combining IR spectroscopy in the presence of CO and EPR spectroscopy, we found that the intrinsic Cu(I) defects of the host react with the guest, forming TCNQ radical anions. This chemistry has profound implications, in particular, with respect to the performance of TCNQ@$Cu_3(BTC)_2$ as an electronic conductor. A decreasing availability of open Cu(II) sites with increasing TCNQ loading proves the coordinative binding of TCNQ to the paddlewheel nodes, and a heterogeneous structure is formed with different TCNQ arrangements and pore environments at low TCNQ loadings. Finally, the combined use of spectroscopic characterization techniques has proven to be, in general, a powerful approach for studying the complex chemistry of host−guest materials.

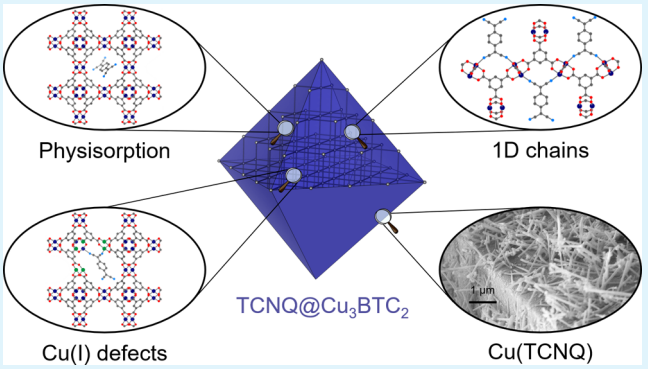

KEYWORDS: *metal−organic frameworks, redox-active guests, defect chemistry, CO probe IR spectroscopy, EPR spectroscopy*

INTRODUCTION

Porous materials play an important role in fundamental research and large-scale industry applications. From activated carbon in exhaust hoods to zeolites for catalytic cracking of hydrocarbons, all materials share high surface areas and pore volumes that allow guest molecules to diffuse and adsorb.[1] A newer class of porous materials named metal−organic frameworks (MOFs) has attracted tremendous attention for use in applications like gas storage, separation, and catalysis.[2,3] Particularly, MOFs with coordinatively unsaturated metal sites, the so-called open metal sites (OMSs), bear great potential compared to their closed coordination-shell analogues as they typically feature high heats of adsorption and intrinsic reactive centers for catalysis.[4−6] Moreover, the OMSs can serve as an anchoring point for other species that are introduced into the MOF postsynthetically, for example, for medical applications.[7] Recently, retrofitting was introduced as a concept, in which metal nodes with OMSs or labile monotopic ligands are bridged by additional linkers to fine-tune physicochemical properties.[8,9] In all cases, the OMS of the MOF is involved in an interaction with the guest molecule, whose nature is typically difficult to assess. Crystallographic characterization, for example, requires a uniform distribution of the guest molecule with long-range order throughout the crystal lattice. In many cases, however, the guest occupies only a portion of the available coordination sites and thus characterizes rather as

Received: September 15, 2019
Accepted: December 6, 2019
Published: December 6, 2019

DOI: 10.1021/acsami.9b16663
ACS Appl. Mater. Interfaces 2020, 12, 1024−1035

a defect to the parent structure that cannot be determined by standard single-crystal X-ray diffraction experiments. Even at high occupancies, structure determination can be challenging due to the small sizes of the crystallites. In some cases, it is possible to track the presence of guests by powder X-ray diffraction (PXRD).[9,10] For example, $Cu_3(BTC)_2$ (HKUST-1, BTC = 1,3,5-benzenetricarboxylate), which is constructed from dimeric Cu(II) paddlewheel units and tritopic BTC linkers, exposes OMSs at the Cu centers after removal of solvents through thermal treatment.[11,12] As the Cu centers are all located in the crystallographic (111) plane, the intensity of the corresponding Bragg reflection is sensitive to adsorption of guests[10] and was used to prove the bidentate binding of TCNQ (7,7,8,8-tetracyanoquinodimethane) to two neighboring Cu paddlewheels (see Figure 1a).[13] This particular host–guest material, TCNQ@$Cu_3(BTC)_2$, arose significant interest in the MOF community in the context of electrical conductivity, including various experimental and computational studies aiming at elucidating the conductivity mechanism.[14−17] However, without a profound understanding of the host–guest chemistry of the material, accurate structure–property relationships cannot be derived. In a previous study, we found that the TCNQ loading by infiltration using methanol as the solvent results in a transformation of $Cu_3(BTC)_2$ to yield Cu(TCNQ).[18] Motivated to exclude any external influences like solvent and moisture, some of us developed a vacuum loading that allows vapor-phase transport of precise molar quantities of TCNQ for adsorption into the framework. Despite the formation of a small amount of the Cu(TCNQ) byproduct on the surface of the MOF crystallites, this approach allows a thorough investigation of the host–guest structure.[13] However, given the intrinsic complexity of the $Cu_3(BTC)_2$ system involving framework defects such as Cu(II)–Cu(I) sites after thermal treatment (i.e., activation),[19,20] interacting with a redox-active guest molecule (see Figure 1b), a comprehensive understanding of the obtained host–guest material in dependence of the synthesis conditions is still not available. For instance, some techniques only provide limited information; X-ray photon absorption (XPS) spectroscopy showed evidence of Cu(I) species[13] but only probes the surface and not the bulk of the crystallites. Therefore, the use of different and more elaborate experimental techniques is necessary. One of these advanced tools is infrared (IR) spectroscopy of adsorbed probe molecules, which has shown great potential as a characterization technique,[21,22] especially for MOFs containing OMSs such as $Cu_3(BTC)_2$.[23,24] Furthermore, electron paramagnetic resonance (EPR) spectroscopy has proven to give important insights about the nature and electronic structure of magnetic species in Cu-based MOFs.[25−30] For example, the magnetic coupling and interactions of Cu(II)–Cu(II) paddlewheel units were characterized in detail by EPR for Cu containing MOFs.[25,26] In addition, EPR was used to study monomeric Cu(II) defects in Cu paddlewheel-based MOFs,[27−29] as well as the adsorption of nonmagnetic or radical species on Zn-doped and pristine $Cu_3(BTC)_2$.[31,32]

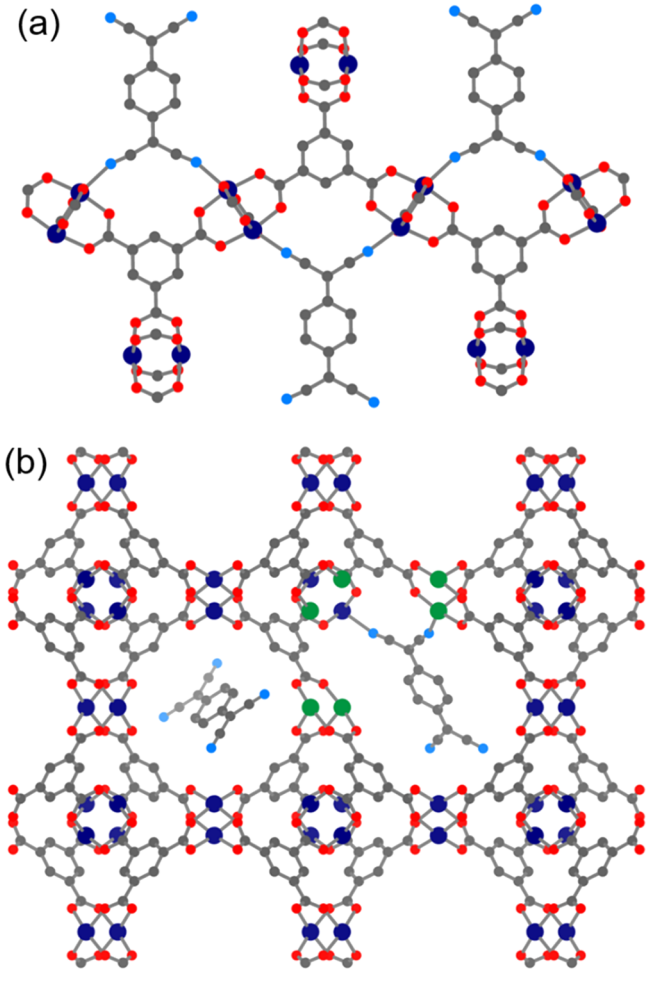

Figure 1. Pore chemistry in TCNQ-loaded $Cu_3(BTC)_2$. (a) In the idealized picture, all Cu paddlewheels are bridged by TCNQ to form one-dimensional arrays along the (111) crystal lattice. (b) For a realistic description of the arrangement of TCNQ as well as noncoordinated TCNQ (left) and TCNQ in interaction with intrinsic framework, defects such as missing linker defects (right) must be considered. Color code: C, gray; O, red; N, blue; Cu, dark blue or green. In particular, Cu(II)–Cu(II) and Cu(II)–Cu(I) paddlewheels are depicted in blue and green, respectively. H atoms are omitted for clarity.

Herein, we aim to draw a clearer picture of the interactions between TCNQ and the host framework, the redox chemistry that is involved during the infiltration, and the pore chemistry of the resulting material. Therefore, we used IR spectroscopy by exploiting the power of carbon monoxide (CO) as a probe molecule to discriminate among framework Cu sites of a very similar nature. By monitoring the vibration frequencies of adsorbed CO, we were able to perform a qualitative and partially quantitative evaluation of the different Cu sites together with an assessment of the local pore environment around the metal centers. In addition, we performed continuous wave (cw) EPR spectroscopy to provide further insights into the presence of molecular radical anions of TCNQ and their correlation with different Cu(II) species, particularly with Cu(II)–Cu(I)-mixed valence paddlewheels.

EXPERIMENTAL SECTION

Synthesis. Pristine $Cu_3(BTC)_2$ was synthesized following the procedure reported in the literature.[12] TCNQ-loaded $Cu_3(BTC)_2$ samples were synthesized following our reported vapor-phase infiltration protocol.[13] Briefly, after thermal activation to remove the solvent (a mixture of *N*,*N*′-dimethylformamide, ethanol, and H_2O) used for solvothermal synthesis and creating the characteristic OMS at the Cu paddlewheel nodes. $Cu_3(BTC)_2$ was physically mixed in a mortar with TCNQ, and then, the mixture was annealed under vacuum in a sealed glass ampoule and heated for 3 days at 180 °C to

DOI: 10.1021/acsami.9b16663
ACS Appl. Mater. Interfaces 2020, 12, 1024−1035

yield the host−guest complex. Distinct amounts of TCNQ were employed to prepare a set of samples with different molar fractions of TCNQ, hereafter referred to as xTCNQ@$Cu_3(BTC)_2$ with $x = n(TCNQ)/n(Cu_3(BTC)_2) = 0.25$, 0.5, and 1.0. During and after the synthesis, the materials were handled under inert conditions (dry Ar or vacuum) and stored in the glovebox to avoid contamination from the atmosphere.

For comparison, a sample was synthesized via solution impregnation following the published synthesis protocol of Talin et al.[44] Therefore, the parent $Cu_3(BTC)_2$ was immersed in a dichloromethane (DCM) solution of TCNQ for 3 days (see the Supporting Information for details). The TCNQ-loaded sample, named *sol*TCNQ@$Cu_3(BTC)_2$, was collected by filtration and dried under vacuum at room temperature.

In Situ IR Spectroscopy. IR spectra were collected in transmission mode on a Bruker Vertex 70 Fourier transform spectrophotometer, equipped with a KBr beamsplitter and a MCT cryodetector, accumulating 32 scans at a 2 cm^{-1} resolution. All samples were examined in the form of thin self-supporting pellets that were prepared inside the glovebox to avoid exposure to the atmosphere. The pellets, mechanically protected with a gold envelope, were placed in a special homemade quartz cell used for operations down to liquid N_2 temperature (i.e., a nominal temperature of 77 K). Transferred out of the glovebox, the cell was connected to a conventional high-vacuum glass line, equipped with a mechanical and a turbo molecular pump (capable of a residual pressure of $P < 10^{-5}$ mbar), which allows activation and in situ adsorption/desorption measurements of the employed molecular probe in a fully controlled atmosphere.[33] Before CO adsorption, each sample was heated at 150 °C under a dynamic vacuum (10^{-5} mbar) for 2 h to remove any potential residual fraction of undesired adsorbates and/or moisture. After the thermal treatment, the material was exposed to CO and cooled down to 77 K. IR spectra were recorded at this temperature, while the CO pressure was gradually decreased to 10^{-4} mbar to obtain an isothermal set of spectra.

EPR Spectroscopy. All cw EPR experiments were performed with a Bruker EMX micro (X-band, 9.4 GHz) spectrometer fitted with a Bruker ER 4119HS cylindrical cavity. Low-temperature experiments were enabled by the Oxford Instruments He cryostat ESR 900. Modulation amplitudes were always set smaller than the smallest peak-to-peak linewidth of transitions in the experimental EPR spectra. Measurements at different microwave (mw) powers ensured that no line shape distortions through saturation occurred for the signals of interest, and that, in case of quantitative experiments, EPR spectra were recorded in the nonsaturating mw power regime. The MATLAB toolbox EasySpin v. 5.2.25,[34] employing the exact diagonalization of the spin Hamiltonian matrix, was used for spectral simulations of the EPR signals. EPR signal intensities of various EPR active species were determined by the double integration of their simulated EPR signals, if their quantification was desired.

All TCNQ-loaded samples for EPR measurements were prepared inside the glovebox by filling the material into an X-band EPR quartz glass tube connected with a high vacuum PTFE valve. The valve was closed and transferred to a vacuum station, where the EPR tube was evacuated and then flame-sealed, keeping the material under inert conditions during each step.

RESULTS AND DISCUSSION

After the synthesis, all materials were carefully characterized to quantitatively determine the TCNQ loading in the MOF structure. Particularly, PXRD data confirmed the successful infiltration (see Figure S2). Standard characterization results of xTCNQ@$Cu_3(BTC)_2$ with $x = 0.1$, 1.0 in 0.1 increments were thoroughly reported in a previous publication.[9] In short, $Cu_3(BTC)_2$ exhibits one small pore of ∼11 Å and two types of large pores of ∼16 Å in diameter. The Cu paddlewheel nodes are oriented in a way that the OMSs at the axial position point to the center of one large pore while being tangential relative to the other large pore (see the Supporting Information for more information). Notably, the synthesis conditions involving noninert solvents at elevated temperatures and a thermal activation of the material promote the formation of intrinsic Cu(I) sites, the so-called modified node defects.[19,35] During the vapor-phase infiltration reaction, TCNQ diffuses into the large pores of $Cu_3(BTC)_2$ and binds preferentially to the available OMSs of two neighboring Cu paddlewheels, as evidenced by PXRD.[18] At the highest possible loading ($x = 1.0$), the large pores can accommodate two molecules of TCNQ while still exhibiting a residual BET-specific surface area of 574 $m^2\ g^{-1}$, that is, about one-third of the pristine $Cu_3(BTC)_2$, still allowing for the adsorption of smaller molecules such as N_2 or CO. During the reaction, a small amount of Cu(TCNQ) forms as a byproduct on the external surface of the crystallites, suggesting an electron transfer from the intrinsic Cu(I) defects of the MOF to TCNQ. The electrical conductivity of the sample correlates quasi-exponentially with the amount of TCNQ employed during the reaction and amounts to 1.5×10^{-4} S cm^{-1} for 1.0TCNQ@$Cu_3(BTC)_2$.[13]

In Situ IR Study of CO Adsorption at 77 K. $Cu_3(BTC)_2$ by itself represents a complex system involving OMSs and a sophisticated defect chemistry. The introduction of TCNQ into the pores adds an additional layer of complexity as it can coordinate to the OMS and accept electrons from the framework. Therefore, the use of standard characterization techniques does not reveal the full picture of this interaction. In situ IR spectroscopy with probe molecules was used in the past and proved to be a powerful technique to shed light on complicated systems,[21,22] such as MOFs containing open metal sites. In particular, the study of CO adsorption at 77 K is one of the more common tools employed to probe the Lewis acidic sites generated by the presence of exposed metal cations.[36,37] For instance, the positively charged Cu(II) species in $Cu_3(BTC)_2$ allow the formation of carbon end Cu(II)−CO adducts, while, in parallel, CO is able to interact with framework Cu(I) defect sites generated by missing carboxylate units (decarboxylation during thermal activation) or with extra-framework Cu(I) species deriving from Cu_2O impurities (e.g., formed during solvothermal synthesis).[20,24,38] Finally, the framework Cu(II) cations in $Cu_3(BTC)_2$ are linked to partially negatively charged carboxylate units, which could constitute a possible interaction site for CO through the formation of oxygen-end adducts as well (organic linker−OC).[39,40] By exploiting the subtle capacity of CO to disclose the existence of sites of such different nature, it is clear how this probe molecule could be useful to clarify the host−guest structure and interactions of xTCNQ@$Cu_3(BTC)_2$. As a general comment, it is worth highlighting that only the species available for interaction with CO are effectively probed, whereas fully coordinated and nonaccessible species cannot be detected. Therefore, this method is not able to probe the Cu(TCNQ) byphase. In addition, it is important that this technique probes the bulk volume of the porous material, and contributions from the external crystallite surface have negligible contributions to the observed IR signals due to the low external surface-to-volume ratio.

$Cu_3(BTC)_2$. Before analyzing the host−guest materials, CO adsorption was carried out on the parent MOF to get a clear picture of the different Cu families. For this purpose, a thin pellet of $Cu_3(BTC)_2$ was prepared inside the glovebox and placed in a homemade IR cell for low-temperature measure-

DOI: 10.1021/acsami.9b16663
ACS Appl. Mater. Interfaces 2020, 12, 1024−1035

ments, as reported in the Experimental Section. After a thermal activation at 150 °C for 2 h, the material was exposed to ~40 mbar CO, cooled down to 77 K, and then gradually evacuated at the same temperature. The isothermal set of spectra is reported in Figure 2 (from dark blue to dark red) in the CO

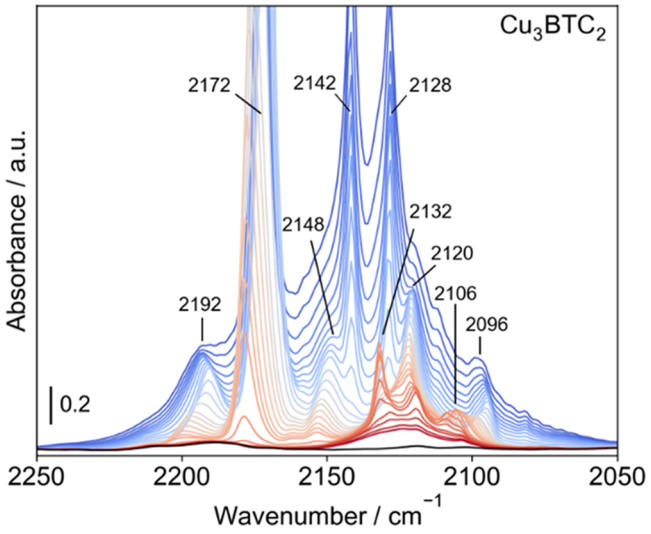

Figure 2. IR spectra of CO adsorbed at 77 K on dehydrated $Cu_3(BTC)_2$ in the CO vibrational mode region. The equilibrium pressure of CO was gradually decreased from ~20 (dark blue) to 10^{-5} mbar (dark red). The spectrum before contact with CO is shown in black. The absorbance is given as a scale bar in the bottom left corner.

vibrational mode spectral range. The spectra of the materials, showing the full mid-IR spectral region before CO contact, are provided in Figure S3.

The whole set of spectra is characterized by an extremely intense and complex envelope of bands due to the CO interaction with the different surface sites. A detail explanation of the various components and of their spectral behavior is reported in the Infrared Spectroscopy section of the Supporting Information. However, to allow a full comprehension of the IR spectra collected after CO adsorption on the *x*TCNQ@$Cu_3(BTC)_2$ host–guest systems, the main spectral features of CO in interaction with pristine $Cu_3(BTC)_2$ are summarized in the following. (i) The out-of-scale band located at around 2172 cm^{-1} is ascribed to the formation of reversible Cu(II)–CO adducts. The peculiar behavior of this band during the outgassing process is due to the gradual conversion of polycarbonyl adsorbate species into monocarbonyls.[24,38] (ii) Considering the interpretation of Drenchev and co-workers, the band at 2192 cm^{-1} could be generated by a different Cu(II)–CO species, whereas the signal at 2148 cm^{-1} (probably stabilized by the presence of the 2192 cm^{-1} component) could be tentatively assigned to CO in interaction with the organic part of the framework.[38] (iii) The bands at around 2120 and 2096 cm^{-1} can be ascribed to the formation of monocarbonyl Cu(I)–CO and Cu(I)–OC (in which the adsorbed CO molecule interacts through the oxygen atom) adducts due to the presence of defective Cu(I) sites.[38,40,41] The component at 2120 cm^{-1} is very stable, persisting until very low CO coverages. (iv) The two signals at 2132 and 2106 cm^{-1} appear in the set of spectra just at a low CO coverage when most of the Cu(II)–CO complexes (band at around 2172 cm^{-1}) is removed and then gradually decrease in intensity upon outgassing. These signals can be tentatively assigned to vibrational modes of bridged Cu(I)–CO–Cu(II) carbonyls in Cu(II)–Cu(I) dimers generated by the presence of missing carboxylate units.[41−43] (v) The two sharp and intense signals at 2142 and 2128 cm^{-1} simultaneously decrease in intensity without any noticeable change in position and are characterized by a very labile nature (they quickly disappear at the early stages of the desorption process). Following the results proposed by Drenchev and co-workers,[38] these bands can be ascribed to CO in interaction with the organic linker via the formation of oxygen-end adducts, presumably with the benzene ring. This assignment is confirmed by observing the modification of some specific spectral features of the organic linker at 1912 and 1896 cm^{-1} during the CO adsorption/desorption experiments with respect to the spectrum of the material before the contact with the probe molecule (see Figure S5).[38] (vi) Finally, at a very low CO coverage, a broad signal appears at 2125 cm^{-1}. The frequency of the component is typical of CO adsorbed on Cu(I) sites of amorphous Cu_2O impurities.[23]

The main IR bands resulting from the interaction of CO with pristine $Cu_3(BTC)_2$ are summarized in Table 1.

xTCNQ@Cu₃(BTC)₂. After the preliminary analysis of the pristine host framework, we turned our attention to the TCNQ-loaded samples aiming to answer three questions: "What happens to the OMSs upon adsorption of TCNQ?", "Do we observe redox processes between Cu(I) defects and TCNQ?", and "How does TCNQ affect the local pore environment of $Cu_3(BTC)_2$?" To this purpose, the CO adsorption at 77 K has been carried out on a series of *x*TCNQ@$Cu_3(BTC)_2$ samples (x = 0.25, 0.5, 1.0) on thin pellets prepared inside the glovebox, as reported in the

Table 1. Assignments of the Main IR Bands Formed upon CO Adsorption on Pristine $Cu_3(BTC)_2$ (See Figure 2)

wavenumber[a]	assignment	CO coverage[b]	ref
2192–2200[c]	polycarbonyl/monocarbonyl Cu(II)–CO	high–low	38
2178	monocarbonyl Cu(II)–CO	medium low	24, 38
2172	polycarbonyl Cu(II)–CO	high–medium high	24, 38
2148[d]	organic linker–OC	high–low	38
2142 and 2128	organic linker–OC	high–medium high	38–40
2132 and 2106	bridged Cu(I)–CO–Cu(II)	low	41–43
2120	monocarbonyl Cu(I)–CO	high–medium low	38, 40, 41
2096	monocarbonyl Cu(I)–OC	high–medium low	40, 41
2125	Cu(I)–CO (of Cu_2O impurities)	low	23

[a]Wavenumber (in cm^{-1}) from this work. [b]CO coverage at which the band is visible. [c]Cu(II)–CO adducts different from the standard ones at 2172–2178 cm^{-1}. [d]Band stabilized by the 2192 cm^{-1} component.

DOI: 10.1021/acsami.9b16663
ACS Appl. Mater. Interfaces 2020, 12, 1024−1035

Experimental Section. The isothermal sets of spectra of the three materials with various TCNQ loadings are reported in Figure 3, showing the CO vibrational mode spectral range. The

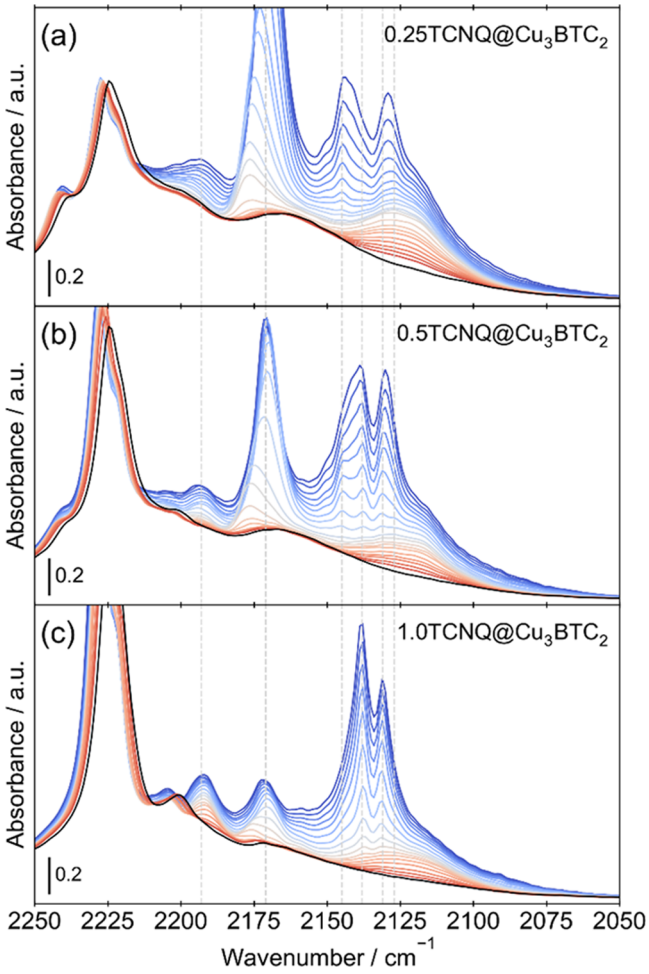

Figure 3. IR spectra of CO adsorbed at 77 K on (a) 0.25TCNQ@$Cu_3(BTC)_2$, (b) 0.5TCNQ@$Cu_3(BTC)_2$, and (c) 1.0TCNQ@$Cu_3(BTC)_2$ in the CO vibrational mode region. The equilibrium pressure of CO was gradually decreased from 16 (dark blue) to 10^{-5} mbar (dark red). The spectra before contact with CO are shown in black. The absorbance is given as a scale bar in the bottom left corner.

spectra have been collected by gradually decreasing the CO equilibrium pressure (from dark blue to dark red curves). For a better comparison, the spectra of the three materials should be normalized to take into account the different pellet thickness. However, the identification of a guest-independent IR band was not possible; unfortunately, the main signals of the host framework change, varying the TCNQ loading. On the other side, different vibration modes exhibit different IR extinction coefficients. Hence, it is clear that no absolute quantitative conclusions can be drawn but simply internal quantitative or qualitative information. Nevertheless, the simple comparison among the intensity ratios of spectral components correlated to different chemical species should allow a clear evaluation of the host−guest interactions.

The spectra of the xTCNQ@$Cu_3(BTC)_2$ samples immediately before the contact of CO are reported in Figure 3 as black curves. Regardless of the TCNQ loading, they are dominated by intense absorptions in the 2250−2180 cm^{-1} range associated with the CN triple bond stretching modes, which characterize the TCNQ guest molecule. Even if the spectra are not normalized, it is evident that bands coherently increase in intensity going from 0.25TCNQ@$Cu_3(BTC)_2$ to 1.0TCNQ@$Cu_3(BTC)_2$. Therefore, it can be reasonably assumed that the three pellets have similar thicknesses and densities and provide comparable results. After the gas admission in the IR cell, an envelope of signals related to the CO interaction with the different surface sites appears. Considering the assignments made for the host framework, the band at around 2170 cm^{-1} is generated by Cu(II)−CO adducts (polycarbonyls or monocarbonyls, depending on the CO coverage). This band decreases considerably as a function of TCNQ loading, indicating a reduced number of available Cu(II) OMSs able to interact with the probe molecule. This trend clearly supports earlier experimental and computational results, suggesting the coordination of TCNQ to the Cu(II) OMSs of $Cu_3(BTC)_2$.[13,44]

Concerning the formation of Cu(I)−CO and Cu(I)−OC adducts (with intrinsic Cu(I) defect sites), the sharp and well-structured bands at 2120 or 2096 cm^{-1}, which were clearly evident in pristine $Cu_3(BTC)_2$, are totally absent, at any CO coverage, in all three samples. The absence of these spectral components is particularly evident in Figure 4b, which compares the spectra of all the materials at a low CO pressure (1 mbar), which is probably the best situation to observe these differences due to the lower reversibility of the signals generated by Cu(I) species. It should be noted that the Cu(I) defect signals are fully absent in the sample with the lowest TCNQ loading (x = 0.25, compare light green and blue curves in Figure 4), suggesting a chemical reaction of these species already induced by the presence of very small amounts of TCNQ. In contrast, in all TCNQ-loaded samples, the extra-framework Cu_2O impurities are always present, as evidenced by the broad and persistent (resistant against prolonged outgassing) component at 2125 cm^{-1}, which seems completely unaffected by the presence of TCNQ. In our previous work, we observed the formation of a byphase of Cu(TCNQ), which requires transfer of an electron to TCNQ and tentatively hypothesized Cu(I) defects being the reducing agent.[9] This previous hypothesis is now strongly supported by the spectroscopic investigation, revealing the absence of the Cu(I) species and the presence of TCNQ radical anions (see the EPR results in the following section; Figure 5).

Looking at the envelope of bands in the region between 2145 and 2125 cm^{-1}, assigned to CO in interaction with the organic backbone (presumably with the benzene ring) via the formation of oxygen-end adducts, the vibrational modes are clearly perturbed by the presence of the large guest molecule inside the MOF cavities. Indeed, at high TCNQ loadings (x = 1.0), the sharp components at 2142 and 2128 cm^{-1} in pristine $Cu_3(BTC)_2$ shift to 2138 and 2131 cm^{-1}, respectively. In contrast, for the materials with lower TCNQ loadings (x = 0.25 and 0.5), these bands are distinctly broader, exhibiting an intermediate situation due to the unambiguous presence of two distinct components for each signal (upon desorption up to four bands are visible in this region). These modifications become evident in Figure 4a, where the spectra of the materials at different TCNQ loadings (from 0 to 1.0), at a medium-high CO coverage, are compared in the spectral range of CO stretching vibrations. The above described spectral changes disclose a different pore environment throughout the TCNQ loading series. While all cavities are empty in pristine $Cu_3(BTC)_2$ (bands at 2142 and 2128 cm^{-1}), in the sample

DOI: 10.1021/acsami.9b16663
ACS Appl. Mater. Interfaces 2020, 12, 1024−1035

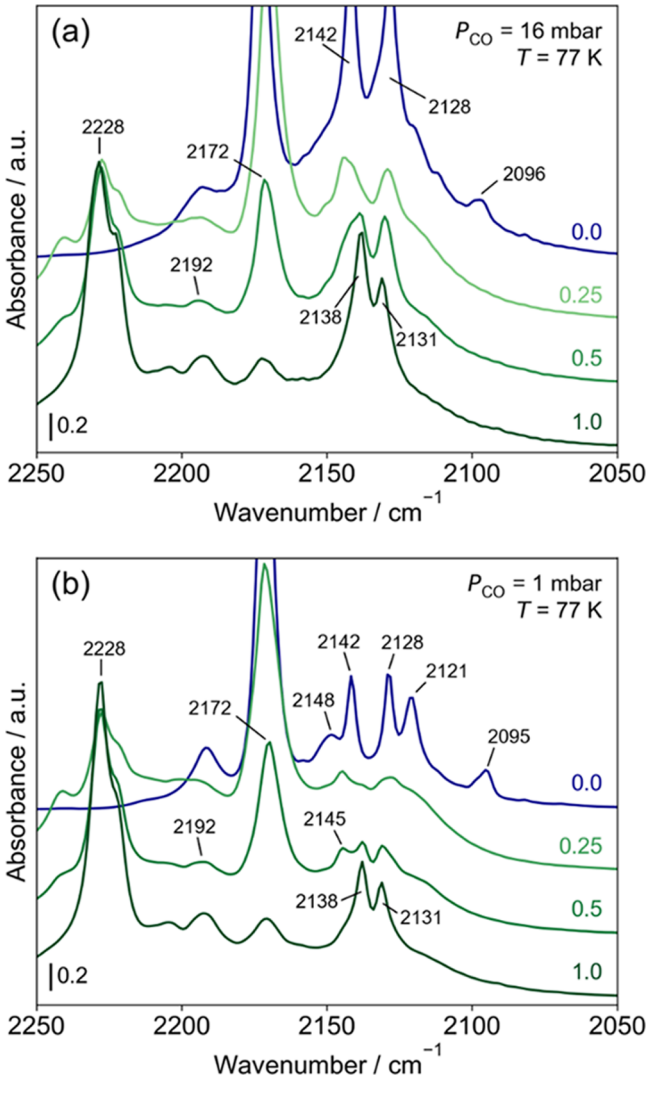

Figure 4. IR spectra of CO adsorbed on pristine $Cu_3(BTC)_2$ (blue) and on different xTCNQ@$Cu_3(BTC)_2$ samples (green) at 77 K in the CO vibrational mode region: comparison at different CO equilibrium pressures. (a) 16 mbar CO. (b) 1 mbar CO. The absorbance is given as a scale bar in the bottom left corner. A vertical offset is applied for clarity.

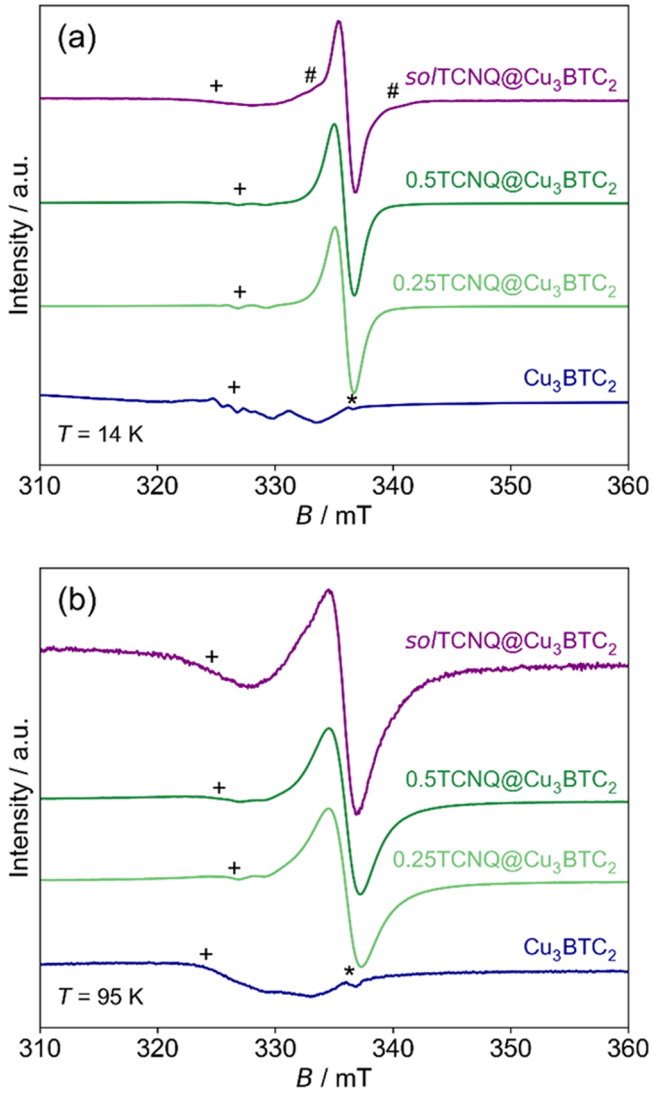

Figure 5. EPR spectra of samples xTCNQ@$Cu_3(BTC)_2$ (x = 0.25, 0.5) (green), *sol*TCNQ@$Cu_3(BTC)_2$ (purple), and pristine $Cu_3(BTC)_2$ (blue) measured at (a) T = 14 K and (b) T = 95 K at a microwave power of 0.02 mW. The maximal signal intensity of the TCNQ-loaded samples was normalized to 1 and set to 0.1 for pristine $Cu_3(BTC)_2$. The pound symbol labels signals that might be attributed to a $TCNQ^-$ species with a larger spectral linewidth. The plus signs label signals of Cu(II) monomers. The asterisk labels a signal that we assign to a free radical impurity at g = 2.000(1).

with x = 1.0 (bands at 2138 and 2121 cm^{-1}), all large pores are occupied with a maximum of two TCNQ molecules.[13,15] In these two well-defined "extreme" cases, the local pore environment is therefore homogeneous. In between these two extremes, samples with x = 0.25 and 0.5 exhibit empty, partially, or completely filled cavities (i.e., containing 0, 1, or 2 TCNQ molecules), resulting in a more complex spectroscopic situation compared to samples with x = 0 and 1.0.

The unequivocal perturbation induced in the organic backbone by the guest TCNQ molecule has been also proven by directly observing the bands at 1912 and 1896 cm^{-1} (assigned to combination modes of the organic framework[38]) in the spectra of the TCNQ loading series before the CO contact, as reported in Figure S5. These vibrations have the maximum intensity in the pristine $Cu_3(BTC)_2$, whereas they gradually disappear upon increasing the TCNQ amount.

Finally, we have to spend a few words to evaluate the spectral behavior of the two IR bands at around 2192 and 2148 cm^{-1}, whose assignment has been reported to be quite controversial in the literature.[24,38] The 2192 cm^{-1} component is always present in all TCNQ-loaded samples, whereas the 2148 cm^{-1} signal gradually disappears by increasing the guest molecule loading (see Figure 4c). This behavior demonstrates the total absence of correlation between these two spectral features, confirming the assignments proposed by Drenchev and co-workers.[38] The band at 2192 cm^{-1} is ascribed to the CO adsorption on a minor fraction of "different" Cu(II) sites, not involved in the interaction with the TCNQ guest molecule, as testified by the high intensity of this band compared to the signal due to standard Cu(II) species (2172 cm^{-1}), especially in the material with the highest TCNQ loading (x = 1.0). In contrast, the component at 2148 cm^{-1} assigned to CO attached to the organic part of the framework is no longer present in 1.0TCNQ@$Cu_3(BTC)_2$ due to the perturbation induced by the TCNQ molecule at its maximum loading.

DOI: 10.1021/acsami.9b16663
ACS Appl. Mater. Interfaces 2020, 12, 1024−1035

Table 2. Assignments of the Main IR Bands Formed upon CO Adsorption on xTCNQ@$Cu_3(BTC)_2$ (See Figure 4)

wavenumber[a]	assignment	xTCNQ@$Cu_3(BTC)_2$[b]
2192[c]	polycarbonyl/monocarbonyl Cu(II)−CO	0.25, 0.5, 1.0
2178	monocarbonyl Cu(II)−CO	0.25 (strong), 0.5 (medium), 1.0 (weak)
2172	polycarbonyl Cu(II)−CO	0.25 (strong), 0.5 (medium), 1.0 (weak)
2148	organic linker−OC	0.25, 0.5
2142 and 2128	organic linker−OC	0.25 (strong), 0.5 (medium)
2138 and 2131	organic linker−OC	0.25 (weak), 0.5 (medium), 0.1 (strong)
2132 and 2106	bridged Cu(I)−CO−Cu(II)	absent
2120	monocarbonyl Cu(I)−CO	absent
2096	monocarbonyl Cu(I)−OC	absent
2125	Cu(I)−CO (of Cu_2O impurities)	0.25, 0.5, 1.0

[a]Wavenumber (in cm^{-1}) from this work. [b]Presence of the band in the xTCNQ@$Cu_3(BTC)_2$ samples and corresponding intensity. [c]Cu(II)−CO adducts different from the standard ones at 2172−2178 cm^{-1}.

The main IR bands resulting from the interaction of CO with xTCNQ@$Cu_3(BTC)_2$ samples are summarized in Table 2.

EPR Spectroscopy. In situ IR spectroscopy results clearly evidence the existence of Cu(I) OMSs in pristine $Cu_3(BTC)_2$ that vanish upon TCNQ loading, indicating a possible electron transfer from Cu(I) ions to TCNQ molecules. To distinctly elucidate the formation of paramagnetic $TCNQ^-$ radicals, we decided to perform cw EPR experiments on some xTCNQ@$Cu_3(BTC)_2$ (x = 0.25, 0.5) samples and compared these results with pristine $Cu_3(BTC)_2$. Indeed, we unambiguously observe EPR signals of $TCNQ^-$ radicals in the vapor-phase-loaded $Cu_3(BTC)_2$ samples, which were absent in pristine $Cu_3(BTC)_2$ (see Figure 5), contrasting with the results by Talin et al. who did not observe any signal of $TCNQ^-$ radicals when they loaded TCNQ into $Cu_3(BTC)_2$ via solution impregnation (TCNQ loading, $x \approx 0.25$).[44] To scrutinize the differences between the two infiltration methods, we synthesized a reference sample, *sol*TCNQ@$Cu_3(BTC)_2$, following its published synthesis protocol, which was then compared with our xTCNQ@$Cu_3(BTC)_2$ samples obtained by vapor-phase infiltration.

The room temperature spectra of pristine $Cu_3(BTC)_2$, xTCNQ@$Cu_3(BTC)_2$ (x = 0.25, 0.5), and *sol*TCNQ@$Cu_3(BTC)_2$ exhibit an isotropic signal at g = 2.15 with a Lorentzian peak-to-peak linewidth of ΔB_{pp} = 92(3) mT (Figure S6). According to previous works,[25,27] we assign these signals to the electron spin S = 1 state of the antiferromagnetically coupled Cu(II)−Cu(II) paddlewheel units, subjected to interdimeric exchange processes. The disappearance of this signal at T = 14 K in all the materials confirms its antiferromagnetic nature (Figure S7). Notably, all TCNQ-loaded samples show an isotropic signal at g = 2.003(2) at T = 14 K (around 335 mT in Figure 5a) with an experimental linewidth of $\Delta B_{pp} \approx 1.6$ mT, typical for radical species due to the presence of $TCNQ^-$.[45] According to the literature, the expected ^{14}N hyperfine (hf) splitting of $TCNQ^-$ anions is of the order of 3 MHz (~0.1 mT)[46,47] which is too small to be resolved in the present case. In contrast to the xTCNQ@$Cu_3(BTC)_2$ samples, the $TCNQ^-$ signal of *sol*TCNQ@$Cu_3(BTC)_2$ exhibits shoulders at the low and high field end, which we tentatively assign to $TCNQ^-$ anions with a larger EPR linewidth. This larger linewidth might indicate a high local concentration of the contributing fraction of $TCNQ^-$ molecules, which leads to dipolar interactions between these species, resulting in a line broadening.

TCNQ Radical Anions. Since we did not observe any signals of $TCNQ^-$ radicals at room temperature (Figure S6), we performed additional EPR experiments at T = 95 K on all TCNQ-loaded samples. Like in the spectra obtained at T = 14 K, the almost isotropic signals of the $TCNQ^-$ radicals at g-values of g = 2.003(2) are visible (Figure 5b). However, their peak-to-peak linewidths increased from ΔB_{pp} = 1.56(23) mT at T = 14 K to ΔB_{pp} = 2.52(40) mT at T = 95 K. By increasing the temperature, the $TCNQ^-$ signals further broaden (e.g., Figure S8) until they totally vanish at room temperature (Figure S6). This observation can be explained by spin−spin interactions between the $TCNQ^-$ radicals with the S = 1 state of nearby Cu(II)−Cu(II) paddlewheel units, which becomes increasingly populated at higher temperature.[25] Indeed, pristine $Cu_3(BTC)_2$ as well as the two TCNQ-loaded xTCNQ@$Cu_3(BTC)_2$ (x = 0.25, 0.5) samples and the reference sample *sol*TCNQ@$Cu_3(BTC)_2$ shows the typical S = 1 signal of magnetically diluted Cu(II)−Cu(II) paddlewheel units at T = 95 K (see Figures S9 to S12),[25,44] verifying that the excited S = 1 state of the paddlewheels had become significantly thermally populated at T = 95 K. This result strongly suggests that the $TCNQ^-$ radicals are located inside the pores of the $Cu_3(BTC)_2$ framework, and the signal is not produced by the Cu(TCNQ) byproduct that was observed to form at the outer surface of the xTCNQ@$Cu_3(BTC)_2$ crystallites.[13]

To roughly estimate the amount of $TCNQ^-$ radicals per paddlewheel unit, the formula for the magnetic susceptibilities χ_M of monomeric electron spin S = 1/2 species and χ_{PW} of dimeric electron spin S = 1 species of the paddlewheels were used, as given in the Supporting Information.[28] Here, the room temperature S = 1 signals of the copper paddlewheels and of the $TCNQ^-$ radicals at T = 75 K were compared with experimental spectra of an ultramarine reference sample that was measured under the same experimental conditions. This accounts for possible differences in the EPR intensities due to different coupling conditions at different temperatures. For each sample, the amount c of $TCNQ^-$ radicals per paddlewheel unit was calculated via

$$c = \frac{I_M(75\ \mathrm{K})}{I_{PW}(295\ \mathrm{K})} \frac{\chi_{PW}(295\ \mathrm{K})}{\chi_M(75\ \mathrm{K})} \quad (1)$$

where I_M(75 K) and I_{PW}(295 K) are the EPR intensities of the $TCNQ^-$ species at T = 75 K and of the S = 1 paddlewheel species at T = 295 K, respectively, as they have been determined by double integrating the corresponding simulated

DOI: 10.1021/acsami.9b16663
ACS Appl. Mater. Interfaces 2020, 12, 1024−1035

Table 3. EPR-Derived Concentration *c* (Number per Paddlewheel Unit) of Different Paramagnetic Species Determined via Eq 1 and Tentative Assignments

Sample	$TCNQ^-$	species A - Cu(II)−Cu(I) paddlewheel	species B_a - defective Cu(II) monomer[a]	species B_b[b] - defective Cu(II) monomer[a]	species C - defective Cu(II) monomer
$Cu_3(BTC)_2$	<0.0002	0.015(8)	0.0013(6)	<0.01	<0.026
0.25TCNQ@ $Cu_3(BTC)_2$	0.025(13)	<0.0004	0.0025(13)	0.0050(25)	<0.0055
0.5TCNQ@ $Cu_3(BTC)_2$	0.016(8)	<0.0012	0.0012(6)	0.012(6)	<0.0068
*sol*TCNQ@ $Cu_3(BTC)_2$	0.010(5)	<0.0025	<0.0003	< 0.006	0.018(9)

[a]Possibly assigned to a broken paddlewheel. [b]Same as species B_a but in higher local concentration.

EPR signals, normalized by means of the ultramarine reference signals. In accordance with the literature, an exchange coupling constant of $J = -370\ cm^{-1}$ was used in the Bleaney−Bowers equation for the magnetic susceptibility of the $S = 1$ spin, which had been determined for the antiferromagnetically coupled Cu paddlewheel units of $Cu_3(BTC)_2\cdot(H_2O)_3$.[25] Following this procedure, we estimate a concentration of 0.025(13), 0.016(8), and 0.010(5) $TCNQ^-$ radicals per paddlewheel units for the samples 0.25TCNQ@$Cu_3(BTC)_2$, 0.5TCNQ@$Cu_3(BTC)_2$, and *sol*TCNQ@$Cu_3(BTC)_2$, respectively (Table 3). These quantitative results prove that a doubling of the TCNQ molecules per paddlewheel unit does not increase the concentration of $TCNQ^-$ radicals, suggesting a scenario where all accessible framework Cu(I) (intrinsic) defects are already oxidized at low TCNQ loadings ($x = 0.25$), and additional TCNQ is adsorbed without undergoing a redox reaction. Consequently, the concentration of $TCNQ^-$ radicals remains at the same order of magnitude in all TCNQ-loaded samples. In contrast to the results reported by Talin et al., we observe a significant amount of $TCNQ^-$ anions in the sample prepared via solution impregnation.[44] This discrepancy could be derived by the slightly different reaction conditions, and more detailed and elaborate experiments to study the materials obtained by TCNQ solution impregnation are suggested. In this study, we show that Cu(I) defects in the crystallite volume act as the reducing agent for the TCNQ guest molecules in both samples obtained via solution impregnation or vapor-phase infiltration. Thereby, the presence of TCNQ radical anions is directly dependent on the intrinsic Cu(I) defect concentration in the pristine MOF, which, in turn, is sensible to the synthesis and activation procedure. Thus, besides the choice of the solvent, which can promote the reduction of TCNQ,[18] the defect concentration of the parent MOF adds another layer of complexity to the synthesis and properties of TCNQ@$Cu_3(BTC)_2$.

Cu(II) Species. At low temperatures, pristine $Cu_3(BTC)_2$ as well as the samples *x*TCNQ@$Cu_3(BTC)_2$ and *sol*TCNQ@$Cu_3(BTC)_2$ exhibits signals of monomeric Cu(II) species, which have a $3d^9$ electron configuration and, therefore, an electron spin of $S = 1/2$ (Figure 6 and Figures S13 and S14). The four measured samples display broad Cu(II) background signals with no resolved $^{63,65}Cu$ (nuclear spin $I = 3/2$) hf splitting, indicative for monomeric Cu(II) species in high local concentration or not well-defined coordination as they might occur at grain or outer boundaries of the MOF crystals or in extra-framework impurity species. One might expect such impurity signals since extra-framework hexaaqua Cu(II) complexes were identified in samples of $Cu_3(BTC)_2$ in a previous work by Pöppl et al.[25] The present samples were activated at higher temperatures and washed for a longer time than in the work of Pöppl et al.[25] However, extra-framework Cu(II) species might still have remained in the present samples, even if they do not occur as hexaaqua complexes due to the potential removal of all water under the harsher

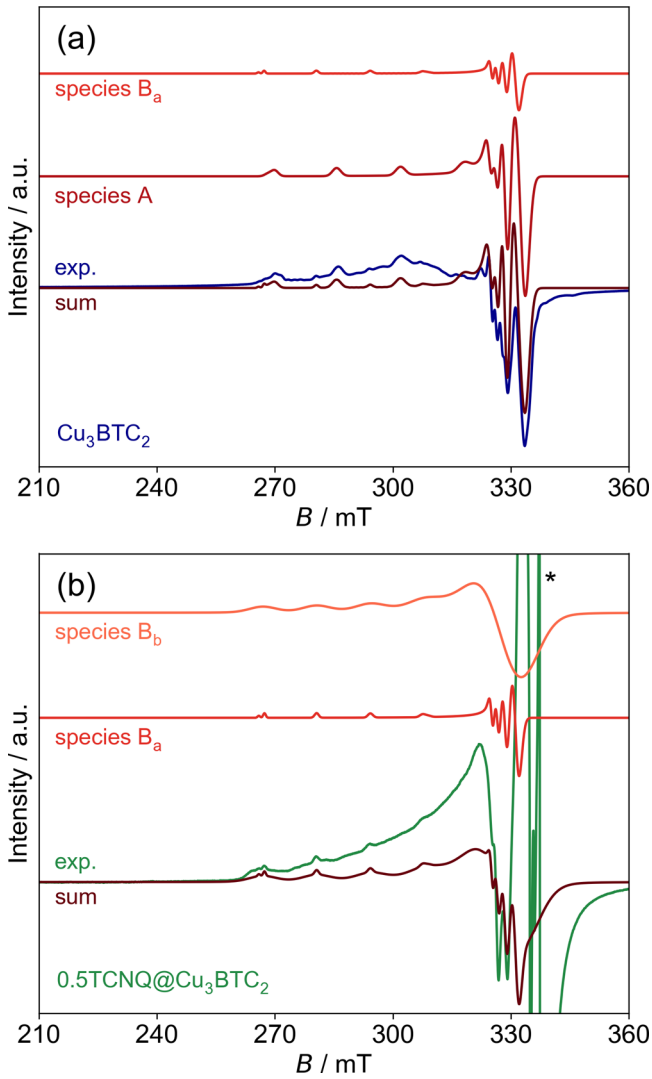

Figure 6. Experimental EPR spectra of (a) pristine $Cu_3(BTC)_2$ (blue) and (b) sample 0.5TCNQ@$Cu_3(BTC)_2$ (green) measured at $T = 14$ K. In panel (a), the sum simulation (brown) is the superposition of the simulated signals of the monomeric Cu(II) species A (dark red) and B_a (red). In panel (b), the sum simulation (brown) is a superposition of the signals of Cu(II) species B_a (red) and B_b (light red). The asterisk labels the saturated signal of $TCNQ^-$ radicals that extends outside the frame and that overlaps with the Cu(II) signals. See Table S1 for simulation parameters.

DOI: 10.1021/acsami.9b16663
ACS Appl. Mater. Interfaces 2020, 12, 1024−1035

activation conditions. In addition, the EPR spectrum of pristine $Cu_3(BTC)_2$ at T = 14 K resolves the g_z ^{63,65}Cu hf transitions of two Cu(II) species A and B_a between 260 and 320 mT as well as the $g_{x,y}$ ^{63,65}hf transitions of species A between 320 and 340 mT (Figure 6a; see Table S1 for the spin Hamilton parameters). Further, minor g_z ^{63,65}Cu hf transitions of other defective Cu(II) species are resolved for pristine $Cu_3(BTC)_2$ at T = 14 K, but their low signal intensities and their overlapping with other hf transitions of different Cu(II) species prevented their clear assignment and determination of their spin Hamiltonian parameters. However, their presence indicates a varied presence of different kinds of well-defined Cu(II) defects in pristine $Cu_3(BTC)_2$.

As explained above for the $TCNQ^-$ radicals, we have determined the concentration of species A in pristine $Cu_3(BTC)_2$ at T = 75 K to 0.015(8) Cu(II) ions per paddlewheel unit (Table 3). Within the experimental error, this concentration is very similar to those determined for the $TCNQ^-$ radicals in all three TCNQ-loaded samples. Importantly, the signal of species A was not observed for the TCNQ-loaded samples anymore (Figure 6b and Figures S13 and S14). The above reported observations suggest that species A represents Cu(II) ions of mixed valence Cu(II)−Cu(I) paddlewheel units in pristine $Cu_3(BTC)_2$. In accordance to the IR results, all diamagnetic Cu(I) ions are oxidized to Cu(II) upon TCNQ loading, and, in parallel, a corresponding fraction of the guest molecule is reduced to $TCNQ^-$. Consequently, the same concentration of $TCNQ^-$ radicals is observed in the loaded samples as Cu(II)−Cu(I) paddlewheel units occur in pristine $Cu_3(BTC)_2$ (Table 3). The magnetic coupling of a potentially formed Cu(II)−Cu(II)−$TCNQ^-$ spin triad is discussed in detail in the Supporting Information. If such spin triads are present in the TCNQ-loaded samples, then the present results indicate a weak exchange interaction between the Cu(II) ion and the axially coordinating $TCNQ^-$ radical without significant distortion of the antiferromagnetic coupling between the two Cu(II) ions and the isotropic $TCNQ^-$ signal. The g- and ^{63}Cu hf-tensor principal values g_z = 2.290(3) and A_z = 0.0170(7) cm^{-1} of species A are typical for Cu(II) ions in square planar to square pyramidal coordination as one would expect for Cu(II) ions in mixed valence paddlewheel units.[48,49] Since Zn(II) and Cu(I) are both $3d^{10}$ ions of similar size, one might expect similar spin Hamiltonian parameters for Cu(II) ions in Cu(II)−Cu(I) and Cu(II)−Zn(II) paddlewheels. Friedländer et al. determined spin Hamiltonian parameters g_z = 2.281(1) and A_z = 0.0187(2) cm^{-1} for Cu(II) ions of mixed metal Cu(II)−Zn(II) paddlewheel units in activated $Cu_{2.965}Zn_{0.035}BTC_2$.[29] Even though they are of the same order of magnitude, they are still different to those of species A and allow no clear statement about their actual nature at this point.

Whereas the monomeric Cu(II) species A is only observed for pristine $Cu_3(BTC)_2$, we observe a second Cu(II) species B_a in pristine $Cu_3(BTC)_2$ as well as the two xTCNQ@$Cu_3(BTC)_2$ (x = 0.25, 0.5) samples (Figure 6 and Figure S13; see Tables S1 for spin Hamiltonian parameters). The Cu(II) concentrations derived by EPR amount to 0.0013(6), 0.0025(13), and 0.0012(6) per paddlewheel unit for pristine $Cu_3(BTC)_2$, 0.25TCNQ@$Cu_3(BTC)_2$, and 0.5TCNQ@$Cu_3(BTC)_2$, respectively (Table 3). The concentration of species B_a is 1 order of magnitude smaller than that of species A. We can only speculate about its nature. In this specific case, species B_a might be ascribed to the single Cu(II) ion of a broken paddlewheel node (i.e., a node with one missing Cu ion) in a well-defined coordination environment, whose presence was reported by Friedländer et al. in Cu paddlewheel-based materials.[28] In samples 0.25TCNQ@$Cu_3(BTC)_2$ and 0.5TCNQ@$Cu_3(BTC)_2$, the g_z ^{63,65}hf transition of species B_a is superimposed by broader lines at the same field position (Figure 6b and Figure S13), which we assign to species B_b. Its identical g_z and A_z values (see Table S1) indicate that species B_b is of the same nature as species B_a but in a higher local concentration or subjected to a larger structural disorder, which leads to considerable broadening of the hf transitions. The estimated concentrations of 0.0050(25) and 0.012(6) Cu(II) ions per paddlewheel in samples 0.25TCNQ@$Cu_3(BTC)_2$ and 0.5TCNQ@$Cu_3(BTC)_2$, respectively (Table 3), imply a correlation between species B_b and the TCNQ loading x. In contrast, the concentration of species B_a remains almost constant, indicating that species B_a is a structural well-defined Cu(II) point defect in a small local concentration. In the spectrum of pristine $Cu_3(BTC)_2$, the superposition with varied ^{63,65}Cu hf transitions of different Cu(II) species at T = 14 K does not allow clear conclusions about the presence or concentration of species B_b. Considering the high local concentration of species B_b, its quantitative correlation with the TCNQ loading amount x, and previous findings showing an increase of the Cu(TCNQ) byphase with x,[13] leads to the hypothesis that species B_b corresponds to the Cu(II) ion of a broken paddlewheel close to the crystallite surface. The missing Cu ion has potentially reacted with TCNQ to form the Cu(TCNQ) surface byphase. Notably, species B_a and B_b are below the detection limit in the EPR spectra of *sol*TCNQ@$Cu_3(BTC)_2$ (Figure S14), while a third Cu(II) species C was observed (Figure S14; see Table S1 for spin Hamiltonian parameters). The relatively large concentration of 0.018(9) Cu(II) ions per paddlewheel unit and less-resolved hf transitions indicate that the treatment of the sample with the TCNQ/DCM solution produces a new type of Cu(II) species in high local concentration or less-defined coordination (Table 3). The above reported results evidence that the distribution of $TCNQ^-$ radicals throughout the pore system is less homogeneous in *sol*TCNQ@$Cu_3(BTC)_2$ compared to the xTCNQ@$Cu_3(BTC)_2$ samples. Therefore, we conclude that the vapor-phase infiltration leads to a more homogeneous TCNQ distribution compared to solution impregnation, which is likely a result of the elevated temperatures and the absence of solvents competing for the available OMSs.

For a better understanding of the different Cu(II) species, we suggest pulsed EPR experiments like electron spin echo envelope modulation (ESEEM) and electron nuclear double resonance (ENDOR) experiments, which might resolve the hf coupling between the Cu(II) electron spin S = 1/2 and the Cu nuclear spin I = 3/2 of the adjacent ^{63,65}Cu(I) ion. Such experiments are currently in progress. Nevertheless, a reduction of TCNQ molecules by Cu(I) ions is strongly indicated by the presented IR and EPR results.

CONCLUSIONS

An advanced spectroscopic characterization study has been carried out by means of IR spectroscopy of adsorbed probe molecules (here, CO) and EPR spectroscopy to disclose the host−guest chemistry of a series of $Cu_3(BTC)_2$ samples containing increasing amounts of TCNQ.

The combined spectroscopic approach together with a comparison of solvent-free vapor-phase infiltration and

DOI: 10.1021/acsami.9b16663
ACS Appl. Mater. Interfaces 2020, 12, 1024−1035

solution impregnation provides substantial answers to the three questions raised at the beginning of this study. By means of in situ IR spectroscopy, we clearly show that the amount of Cu(II) OMSs in $Cu_3(BTC)_2$ decreases monotonically by increasing the guest loading because of the occupation by TCNQ. In combination with our previous powder diffraction data,[13] the presented results dispelled any doubt about the coordination of TCNQ to the Cu(II) dimers of the paddlewheel units. Moreover, the IR data revealed a homogeneous pore environment for the pristine and fully loaded MOF (x = 1.0; i.e., two TCNQs per large pore), whereas intermediate samples exhibited a more heterogeneous, variegated TCNQ distribution inside the microporous cavities. In addition, both IR and EPR data evidenced the presence of intrinsic Cu(I) framework defects in the volume of pristine $Cu_3(BTC)_2$ that disappear immediately upon exposure to even small TCNQ amounts. In return, the presence of TCNQ radical anions becomes evident in all TCNQ-loaded samples. Remarkably, the radical concentration in the TCNQ-loaded samples correlates quantitatively with the Cu(II)−Cu(I) defect concentration in the parent MOF, evidencing an electron transfer from the Cu(I) defects to TCNQ. Additional pulsed EPR measurements are currently in progress to get further insights into the nature of the different Cu(II) species.

The results obtained during this study have profound implication for the fabrication and the understanding of the physical origin of the electronic conductivity and performance of devices based on TCNQ@$Cu_3(BTC)_2$. We find that the framework Cu(I) defect concentration directly correlates with the TCNQ radical anion concentration, thereby introducing additional charge carriers into the system, which is typically associated with an increase in electrical conductivity. In fact, the maximum $TCNQ^-$ concentration is already reached at low loadings, which would result in a plateau of the conductivity at higher loadings if the introduced charge carrier was the only contribution to the conductivity. This contrasts with the experimental results.[13,44] An increased charge mobility due to neutral TCNQ in the pores, or contributions from a Cu(TCNQ) surface byphase that forms under certain conditions,[13,18] must also be taken into account when studying the electronic properties of these materials.[14,15,17,44] The use of carefully fabricated defect-free $Cu_3(BTC)_2$ thin films[50,51] as the starting material for the infiltration reaction under very mild conditions (low temperature, inert solvent) will likely lead to a host−guest material without the formation of TCNQ radicals. In a similar way, defect-free bulk materials should be accessible by optimization of the synthetic protocol; however, mild activation procedures to generate the OMSs without Cu(I) defect formation are scarce or even absent.[40,52−54] The present system is yet another example where the defect chemistry of MOFs has a significant impact on the material properties and underlines the importance of advancing the research field of defect-engineered MOFs.[35,55]

At this point, we like to highlight our recent computational study on structurally retrofitting metal−organic frameworks with cross-linkers (CL), in particular, Cu paddlewheel-based systems such as CL@$Cu_3(BTC)_2$ and the expansion to CL@NOTT-100 and CL@NOT-101.[9] A library of 20 CLs with binding properties similar to TCNQ was evaluated. We suggest that the chemical interaction of these potentially noninnocent guest molecules with Cu paddlewheel-based MOFs beyond the simple coordination to the open copper sites may be as complex as the present case of $Cu_3(BTC)_2$ (HKUST-1), and it may be elucidated in detail following the methodology as we described above.

As a final, and more general, remark, it is worth highlighting that a high precision inorganic solid-state synthesis together with the application of a suite of complementary techniques of spectroscopic characterization represents a powerful approach to study the subtle, and frequently unexpectedly complex, chemistry of synergetic Guest@MOF systems,[54] in general.

■ ASSOCIATED CONTENT

Supporting Information

The Supporting Information is available free of charge at https://pubs.acs.org/doi/10.1021/acsami.9b16663.

Information about the synthesis, powder X-ray diffraction, IR, and EPR spectroscopy (PDF)

■ AUTHOR INFORMATION

Corresponding Authors

*E-mail: valentina.crocella@unito.it (V.C.).
*E-mail: roland.fischer@tum.de (R.A.F.).

ORCID

Matthias Mendt: 0000-0002-1295-0228
Valentina Crocellà: 0000-0002-3606-8424
Roland A. Fischer: 0000-0002-7532-5286

Author Contributions

The manuscript was written through contributions of all authors. All authors have given approval to the final version of the manuscript.

Funding

DFG SPP1928 (COORNETs).

Notes

The authors declare no competing financial interest.

■ ACKNOWLEDGMENTS

The authors would like to thank Silvia Bordiga for insightful discussions. C.S. acknowledges his scholarships from the German Academic Scholarship Foundation and from the German Chemical Industry Fund (FCI). This work was supported by the German Research Foundation Priority Program 1928 "CCORNETs" (www.coornets.tum.de).

■ REFERENCES

(1) Weckhuysen, B. M.; Yu, J. Recent Advances in Zeolite Chemistry and Catalysis. *Chem. Soc. Rev.* **2015**, *44*, 7022−7024.
(2) Slater, A. G.; Cooper, A. I. Function-Led Design of New Porous Materials. *Science* **2015**, *348*, aaa8075.
(3) Zhou, H.-C.; Kitagawa, S. Metal−Organic Frameworks (MOFs). *Chem. Soc. Rev.* **2014**, *43*, 5415−5418.
(4) Chen, C.; Lee, Y.-R.; Ahn, W.-S. CO_2 Adsorption Over Metal-Organic Frameworks: A Mini Review. *J. Nanosci. Nanotechnol.* **2016**, *16*, 4291−4301.
(5) Hall, J. N.; Bollini, P. Structure, Characterization, and Catalytic Properties of Open-Metal Sites in Metal Organic Frameworks. *React. Chem. Eng.* **2019**, *4*, 207−222.
(6) Liu, J.; Chen, L.; Cui, H.; Zhang, J.; Zhang, L.; Su, C.-Y. Applications of Metal−Organic Frameworks in Heterogeneous Supramolecular Catalysis. *Chem. Soc. Rev.* **2014**, *43*, 6011−6061.
(7) Souza, B. E.; Rudić, S.; Titov, K.; Babal, A. S.; Taylor, J. D.; Tan, J.-C. Guest−Host Interactions of Nanoconfined Anti-Cancer Drug in Metal−Organic Framework Exposed by Terahertz Dynamics. *Chem. Commun.* **2019**, *55*, 3868−3871.

DOI: 10.1021/acsami.9b16663
ACS Appl. Mater. Interfaces 2020, 12, 1024−1035

(8) Kapustin, E. A.; Lee, S.; Alshammari, A. S.; Yaghi, O. M. Molecular Retrofitting Adapts a Metal−Organic Framework to Extreme Pressure. *ACS Cent. Sci.* **2017**, *3*, 662−667.
(9) Schneider, C.; Bodesheim, D.; Keupp, J.; et al. Retrofitting metal-organic frameworks. *Nat. Commun.* **2019**, *10*, 4921.
(10) Schlichte, K.; Kratzke, T.; Kaskel, S. Improved Synthesis, Thermal Stability and Catalytic Properties of the Metal-Organic Framework Compound $Cu_3(BTC)_2$. *Microporous Mesoporous Mater.* **2004**, *73*, 81−88.
(11) Chui, S. S.-Y.; Lo, S. M.-F.; Charmant, J. P. H.; Orpen, A. G.; Williams, I. D. Chemically Functionalizable Nanoporous Material $[Cu_3(TMA)_2(H_2O)_3]_n$. *Science* **1999**, *283*, 1148−1150.
(12) Bhunia, M. K.; Hughes, J. T.; Fettinger, J. C.; Navrotsky, A. Thermochemistry of Paddle Wheel MOFs: Cu-HKUST-1 and Zn-HKUST-1. *Langmuir* **2013**, *29*, 8140−8145.
(13) Schneider, C.; Ukaj, D.; Koerver, R.; Talin, A. A.; Kieslich, G.; Pujari, S. P.; Zuilhof, H.; Janek, J.; Allendorf, M. D.; Fischer, R. A. High Electrical Conductivity and High Porosity in a Guest@MOF Material: Evidence of TCNQ Ordering within Cu_3 BTC_2 Micropores. *Chem. Sci.* **2018**, *9*, 7405−7412.
(14) Neumann, T.; Liu, J.; Wächter, T.; Friederich, P.; Symalla, F.; Welle, A.; Mugnaini, V.; Meded, V.; Zharnikov, M.; Wöll, C.; Wenzel, W. Superexchange Charge Transport in Loaded Metal Organic Frameworks. *ACS Nano* **2016**, *10*, 7085−7093.
(15) Erickson, K. J.; Léonard, F.; Stavila, V.; Foster, M. E.; Spataru, C. D.; Jones, R. E.; Foley, B. M.; Hopkins, P. E.; Allendorf, M. D.; Talin, A. A. Thin Film Thermoelectric Metal-Organic Framework with High Seebeck Coefficient and Low Thermal Conductivity. *Adv. Mater.* **2015**, *27*, 3453−3459.
(16) Hendon, C. H.; Walsh, A. Chemical Principles Underpinning the Performance of the Metal−Organic Framework HKUST-1. *Chem. Sci.* **2015**, *6*, 3674−3683.
(17) Chen, X.; Wang, Z.; Hassan, Z. M.; Lin, P.; Zhang, K.; Baumgart, H.; Redel, E. Seebeck Coefficient Measurements of Polycrystalline and Highly Ordered Metal-Organic Framework Thin Films. *ECS J. Solid State Sci. Technol.* **2017**, *6*, P150−P153.
(18) Thürmer, K.; Schneider, C.; Stavila, V.; Friddle, R. W.; Léonard, F.; Fischer, R. A.; Allendorf, M. D.; Talin, A. A. Surface Morphology and Electrical Properties of Cu_3BTC_2 Thin Films Before and After Reaction with TCNQ. *ACS Appl. Mater. Interfaces* **2018**, *10*, 39400−39410.
(19) Nijem, N.; Bluhm, H.; Ng, M. L.; Kunz, M.; Leone, S. R.; Gilles, M. K. Cu^{1+} in HKUST-1: Selective Gas Adsorption in the Presence of Water. *Chem. Commun.* **2014**, *50*, 10144−10147.
(20) Szanyi, J.; Daturi, M.; Clet, G.; Baer, D. R.; Peden, C. H. F. Well-Studied Cu−BTC Still Serves Surprises: Evidence for Facile Cu^{2+}/Cu^{+} Interchange. *Phys. Chem. Chem. Phys.* **2012**, *14*, 4383.
(21) Lamberti, C.; Zecchina, A.; Groppo, E.; Bordiga, S. Probing the Surfaces of Heterogeneous Catalysts by in Situ IR Spectroscopy. *Chem. Soc. Rev.* **2010**, *39*, 4951.
(22) Vimont, A.; Thibault-Starzyk, F.; Daturi, M. Analysing and Understanding the Active Site by IR Spectroscopy. *Chem. Soc. Rev.* **2010**, *39*, 4928.
(23) Prestipino, C.; Regli, L.; Vitillo, J. G.; Bonino, F.; Damin, A.; Lamberti, C.; Zecchina, A.; Solari, P. L.; Kongshaug, K. O.; Bordiga, S. Local Structure of Framework Cu(II) in HKUST-1 Metallorganic Framework: Spectroscopic Characterization upon Activation and Interaction with Adsorbates. *Chem. Mater.* **2006**, *18*, 1337−1346.
(24) Bordiga, S.; Regli, L.; Bonino, F.; Groppo, E.; Lamberti, C.; Xiao, B.; Wheatley, P. S.; Morris, R. E.; Zecchina, A. Adsorption Properties of HKUST-1 toward Hydrogen and Other Small Molecules Monitored by IR. *Phys. Chem. Chem. Phys.* **2007**, *9*, 2676.
(25) Pöppl, A.; Kunz, S.; Himsl, D.; Hartmann, M. CW and Pulsed ESR Spectroscopy of Cupric Ions in the Metal−Organic Framework Compound $Cu_3(BTC)_2$. *J. Phys. Chem. C* **2008**, *112*, 2678−2684.
(26) Šimėnas, M.; Kobalz, M.; Mendt, M.; Eckold, P.; Krautscheid, H.; Banys, J.; Pöppl, A. Synthesis, Structure, and Electron Paramagnetic Resonance Study of a Mixed Valent Metal−Organic Framework Containing Cu_2 Paddle-Wheel Units. *J. Phys. Chem. C* **2015**, *119*, 4898−4907.
(27) Jee, B.; Eisinger, K.; Gul-E-Noor, F.; Bertmer, M.; Hartmann, M.; Himsl, D.; Pöppl, A. Continuous Wave and Pulsed Electron Spin Resonance Spectroscopy of Paramagnetic Framework Cupric Ions in the Zn(II) Doped Porous Coordination Polymer $Cu_{3-x}Zn_x(BTC)_2$. *J. Phys. Chem. C* **2010**, *114*, 16630−16639.
(28) Friedländer, S.; Šimėnas, M.; Kobalz, M.; Eckold, P.; Ovchar, O.; Belous, A. G.; Banys, J.; Krautscheid, H.; Pöppl, A. Single Crystal Electron Paramagnetic Resonance with Dielectric Resonators of Mononuclear Cu^{2+} Ions in a Metal−Organic Framework Containing Cu_2 Paddle Wheel Units. *J. Phys. Chem. C* **2015**, *119*, 19171−19179.
(29) Friedländer, S.; Petkov, P. S.; Bolling, F.; Kultaeva, A.; Böhlmann, W.; Ovchar, O.; Belous, A. G.; Heine, T.; Pöppl, A. Continuous-Wave Single-Crystal Electron Paramagnetic Resonance of Adsorption of Gases to Cupric Ions in the Zn(II)-Doped Porous Coordination Polymer $Cu_{2.965}Zn_{0.035}(BTC)_2$. *J. Phys. Chem. C* **2016**, *120*, 27399−27411.
(30) Pöppl, A.; Jee, B.; Icker, M.; Hartmann, M.; Himsl, D. Untersuchungen Zur Chemischen Stabilität von $Cu_3(BTC)_2$ (HKUST-1) Durch N_2-Adsorption, Rönt-genpulverdiffraktometrie Und EPR-Spektroskopie. *Chem. Ing. Tech.* **2010**, *82*, 1025−1029.
(31) Jee, B.; Koch, K.; Moschkowitz, L.; Himsl, D.; Hartman, M.; Pöppl, A. Electron Spin Resonance Study of Nitroxide Radical Adsorption at Cupric Ions in the Metal−Organic Framework Compound Cu_3 $(BTC)_2$. *J. Phys. Chem. Lett.* **2011**, *2*, 357−361.
(32) Jee, B.; St. Petkov, P.; Vayssilov, G. N.; Heine, T.; Hartmann, M.; Pöppl, A. A Combined Pulsed Electron Paramagnetic Resonance Spectroscopic and DFT Analysis of the $^{13}CO_2$ and ^{13}CO Adsorption on the Metal−Organic Framework $Cu_{2.97}Zn_{0.03}(BTC)_2$. *J. Phys. Chem. C* **2013**, *117*, 8231−8240.
(33) Crocellà, V.; Tabanelli, T.; Vitillo, J. G.; Costenaro, D.; Bisio, C.; Cavani, F.; Bordiga, S. A Multi-Technique Approach to Disclose the Reaction Mechanism of Dimethyl Carbonate Synthesis over Amino-Modified SBA-15 Catalysts. *Appl. Catal,. B* **2017**, *211*, 323.
(34) Stoll, S.; Schweiger, A. EasySpin, a Comprehensive Software Package for Spectral Simulation and Analysis in EPR. *J. Magn. Reson.* **2006**, *178*, 42−55.
(35) Dissegna, S.; Epp, K.; Heinz, W. R.; Kieslich, G.; Fischer, R. A. Defective Metal-Organic Frameworks. *Adv. Mater.* **2018**, *30*, 1704501−1704524.
(36) Volkringer, C.; Leclerc, H.; Lavalley, J.-C.; Loiseau, T.; Férey, G.; Daturi, M.; Vimont, A. Infrared Spectroscopy Investigation of the Acid Sites in the Metal−Organic Framework Aluminum Trimesate MIL-100(Al). *J. Phys. Chem. C* **2012**, *116*, 5710−5719.
(37) Chavan, S.; Vitillo, J. G.; Groppo, E.; Bonino, F.; Lamberti, C.; Dietzel, P. D. C.; Bordiga, S. CO Adsorption on CPO-27-Ni Coordination Polymer: Spectroscopic Features and Interaction Energy. *J. Phys. Chem. C* **2009**, *113*, 3292−3299.
(38) Drenchev, N.; Ivanova, E.; Mihaylov, M.; Hadjiivanov, K. CO as an IR Probe Molecule for Characterization of Copper Ions in a Basolite C300 MOF Sample. *Phys. Chem. Chem. Phys.* **2010**, *12*, 6423−6427.
(39) Bonino, F.; Lamberti, C.; Chavan, S.; Vitillo, J. G.; Bordiga, S.. Chapter 4. Characterization of MOFs. 1. Combined Vibrational and Electronic Spectroscopies. In *Metal Organic Frameworks as Heterogeneous Catalysts*; The Royal Society of Chemistry: 2013, pp 76−142.
(40) St. Petkov, P.; Vayssilov, G. N.; Liu, J.; Shekhah, O.; Wang, Y.; Wöll, C.; Heine, T. Defects in MOFs: A Thorough Characterization. *ChemPhysChem* **2012**, *13*, 2025−2029.
(41) Areán, C. O.; Delgado, M. R.; Frolich, K.; Bulánek, R.; Pulido, A.; Bibiloni, G. F.; Nachtigall, P. Computational and Fourier Transform Infrared Spectroscopic Studies on Carbon Monoxide Adsorption on the Zeolites Na-ZSM-5 and K-ZSM-5: Evidence of Dual-Cation Sites. *J. Phys. Chem. C* **2008**, *112*, 4658−4666.
(42) Bulanek, R.; Frolich, K.; Cicmanec, P.; Nachtigallova, D.; Pulido, A.; Nachtigall, P. Combined Experimental and Theoretical Investigations of Heterogeneous Dual Cation Sites in Cu,M-FER Zeolites. *J. Phys. Chem. C* **2011**, *115*, 13312−13321.

DOI: 10.1021/acsami.9b16663
ACS Appl. Mater. Interfaces 2020, 12, 1024−1035

(43) Frolich, K.; Koudelkova, E.; Frydova, E.; Bulanek, R. The Quantity of Cu^{+} Ions Forming Isolated and Bridged Carbonyl Complexes in FER Zeolites Determined by IR Spectroscopy. *Vib. Spectrosc.* **2012**, *58*, 146−152.
(44) Talin, A. A.; Centrone, A.; Ford, A. C.; Foster, M. E.; Stavila, V.; Haney, P.; Kinney, R. A.; Szalai, V.; El Gabaly, F.; Yoon, H. P.; Léonard, F.; Allendorf, M. D. Tunable Electrical Conductivity in Metal-Organic Framework Thin-Film Devices. *Science* **2014**, *343*, 66−69.
(45) Schwertdfeger, C. F. Low Temperature EPR Study of the "Impurity" Resonances in $(TCNQ)^{-}$ and $(TCNQ)^{-}_{2}$ Salts. *Solid State Commun.* **1977**, *23*, 621−622.
(46) Bell, S. E.; Field, J. S.; Haines, R. J.; Moscherosch, M.; Matheis, W.; Kaim, W. Novel and Stable Metal-Metal-Bonded Diruthenium(I) Complexes Containing TCNX0/.Bul.- in Both the Inner and the Outer Coordination Sphere (TCNX = TCNE, TCNQ). A Combined EPR/ENDOR-, UV/Visible/near-IR-, and IR-Spectroscopic and Electrochemical Investigation. *Inorg. Chem.* **1992**, *31*, 3269−3276.
(47) Flandrois, S.; Boissonade, J. EPR Fine Structure and Spin Densities in TCNQ Salts. *Chem. Phys. Lett.* **1978**, *58*, 596−600.
(48) Hathaway, B. J.; Billing, D. E. The Electronic Properties and Stereochemistry of Mono-Nuclear Complexes of the Copper(II) Ion. *Coord. Chem. Rev.* **1970**, *5*, 143−207.
(49) Tominaga, H.; Ono, Y.; Keii, T. Spectroscopic Study of Cu(II) Ions Supported on Silica Gel by Cation Exchange Method. *J. Catal.* **1975**, *40*, 197−202.
(50) Gu, Z.-G.; Pfriem, A.; Hamsch, S.; Breitwieser, H.; Wohlgemuth, J.; Heinke, L.; Gliemann, H.; Wöll, C. Transparent Films of Metal-Organic Frameworks for Optical Applications. *Microporous Mesoporous Mater.* **2015**, *211*, 82−87.
(51) Delen, G.; Ristanović, Z.; Mandemaker, L. D. B.; Weckhuysen, B. M. Mechanistic Insights into Growth of Surface-Mounted Metal-Organic Framework Films Resolved by Infrared (Nano-) Spectroscopy. *Chem. Eur. J.* **2018**, *24*, 187−195.
(52) Mendt, M.; Gutt, F.; Kavoosi, N.; Bon, V.; Senkovska, I.; Kaskel, S.; Pöppl, A. EPR Insights into Switchable and Rigid Derivatives of the Metal−Organic Framework DUT-8(Ni) by NO Adsorption. *J. Phys. Chem. C* **2016**, *120*, 14246−14259.
(53) Bae, J.; Choi, J. S.; Hwang, S.; Yun, W. S.; Song, D.; Lee, J.; Jeong, N. C. Multiple Coordination Exchanges for Room-Temperature Activation of Open-Metal Sites in Metal−Organic Frameworks. *ACS Appl. Mater. Interfaces* **2017**, *9*, 24743−24752.
(54) Allendorf, M. D.; Medishetty, R.; Fischer, R. A. Guest Molecules as a Design Element for Metal−Organic Frameworks. *MRS Bull.* **2016**, *41*, 865−869.
(55) Fang, Z.; Bueken, B.; De Vos, D. E.; Fischer, R. A. Defect-Engineered Metal-Organic Frameworks. *Angew. Chem., Int. Ed.* **2015**, *54*, 7234−7254.

DOI: 10.1021/acsami.9b16663
ACS Appl. Mater. Interfaces 2020, 12, 1024−1035